Minerals Engineering 219 (2024) 109059

Contents lists available at ScienceDirect

Minerals Engineering

journal homepage: www.elsevier.com/locate/mineng

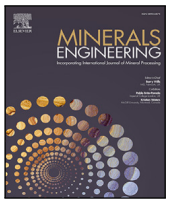

State and parameter estimation of a dynamic froth flotation model using industrial data

Jaco-Louis Venter, Johan Derik le Roux *, Ian Keith Craig

Department of Electrical, Electronic and Computer Engineering, University of Pretoria, Pretoria, South Africa

ARTICLE INFO

Keywords:
Dynamic model validation
Froth flotation
Moving horizon estimator
Mineral processing
State and parameter estimation

ABSTRACT

This paper investigates an observable dynamic model of froth flotation circuits aimed at online state and parameter estimation and model-based control. The aim is to estimate the model states and parameters online from industrial data. However, in light of limitations in the plant data, additional model analysis is conducted. It is shown that without online compositional measurements, only the states and parameters of a reduced model can be estimated online. The reduced model lumps all recovery mechanisms into a single empirical equation. The reduced model is used to develop a moving horizon estimator (MHE) which is implemented on the industrial data. The state and parameter estimates from the MHE are used to evaluate the model prediction accuracy over a receding control horizon as would be done in model predictive control (MPC). Given the uncertainty of the available data, unmeasured disturbances and missing online measurements, the estimation and prediction results are reasonably accurate, at least in a qualitative sense. If accurate and reliable online measurements are available for estimation, the reduced model shows potential to be used for long-term model-based supervisory control of a flotation circuit.

1. Introduction

Froth flotation is currently one of the largest mineral separation techniques in use. Its scale means that even slight efficiency improvements could have a large impact on the global minerals processing industry (Quintanilla et al., 2021a). As such, the control and optimisation of flotation circuits have received considerable attention since its development (Bascur Riquelme, 1982; Shean and Cilliers, 2011; Oosthuizen et al., 2017; Quintanilla et al., 2021a). It is well-established that traditional proportional and integral (PI) control and other single-input single-output (SISO) control methods are not sufficient to properly control flotation beyond base level stabilisation or regulatory control (Shean and Cilliers, 2011; Quintanilla et al., 2021a) and there is a need for more advanced control techniques, such as model predictive control (MPC), to increase the efficiency of flotation.

At the time of their review, Bergh and Yianatos (2011) identified the lack of suitable dynamic models, quality online measurements of key variables and acceptable regulatory control as the main obstacles to the successful use of MPC in flotation. The long-term implementation of MPC requires models that capture the important system dynamics and have a low computational processing burden for online controller implementation. These models should also be easily maintainable from limited online measurements, as detailed sampling campaigns are costly and time-consuming (Shean et al., 2018; Oosthuizen, 2023; Quintanilla et al., 2021a; Steyn and Sandrock, 2021).

Recently, significant research effort has been aimed at addressing these issues (Brooks and Koorts, 2017; Oosthuizen et al., 2017; Shean et al., 2018; Brooks et al., 2019; Quintanilla et al., 2021a,c,b; Steyn and Sandrock, 2021; Oosthuizen, 2023; Quintanilla et al., 2023). Two of the most recent dynamic models of flotation circuits aimed at MPC were proposed by Oosthuizen et al. (2021) and Quintanilla et al. (2021c).

Quintanilla et al. (2021c) developed a primarily phenomenological model that includes the froth physics and interaction between pulp and froth. The model was validated by Quintanilla et al. (2021b) using extensive experiments on a single, well-instrumented laboratory scale flotation cell. The feed properties and reagent dosages were kept constant and parameter values were assumed to remain constant. Without tests where these conditions were varied, it is not known how well the model extends to other operation conditions and how much the parameters would have to change. Quintanilla et al. (2023) used the model to develop an economic MPC (E-MPC) strategy, demonstrating very good control performance in simulation. They mention that there is still the need to develop a state estimator to facilitate the implementation of the E-MPC on a laboratory flotation bank.

The model first published in Oosthuizen et al. (2021) and refined in Oosthuizen (2023) combines established phenomenological models and mass balances with empirical models of phenomena not understood very well such as froth dynamics. Importantly, the model states

* Corresponding author.
E-mail address: derik.leroux@up.ac.za (J.D. le Roux).

https://doi.org/10.1016/j.mineng.2024.109059
Received 6 May 2024; Received in revised form 3 October 2024; Accepted 15 October 2024
Available online 24 October 2024

and parameters are observable and identifiable from the measurements generally available on industrial flotation plants (Oosthuizen et al., 2021). Observability (or identifiability in the case of parameters) is a mathematical property of a model which means that the model states (or parameters) can be estimated from the measured plant variables (Villaverde et al., 2019). This is a crucial part of an MPC strategy where state-feedback is necessary to ensure closed-loop feedback control. By ensuring observability and identifiability, the states and parameters of the model of Oosthuizen (2023) which cannot be measured directly can be estimated in real time from online plant measurements. The rationale of this modelling approach is that while the empirical models do not capture the effect of all impacting factors on the flotation process, the online estimation of their parameters can, to some extent, capture the effect of these factors, as long as they do not change too rapidly (Oosthuizen, 2023). The neglected factors include, among others, the effect of chemical reagent dosages and particle size distribution on the flotation rate and froth stability, which are not commonly modelled in literature (Oosthuizen et al., 2021; Venter et al., 2022).

Oosthuizen (2023) modified the empirical air recovery model structure of Oosthuizen et al. (2021) to better correlate with the observed behaviour of the peak in air recovery, as recorded in Hadler et al. (2010, 2012). The parameters that determine the optimal J_g value and maximum achievable air recovery in each cell were also allowed to vary between cells, as this is more akin to what is seen in industrial flotation circuits. Oosthuizen (2023) fitted the model states and parameters to steady-state plant data from Hadler et al. (2010). He shows in simulation that good parameter estimation and control results are possible, assuming online compositional analysers are available for estimation purposes. While such analysers are used on some flotation circuits (Brooks and Koorts, 2017), they are still not common (Shean and Cilliers, 2011; Oosthuizen et al., 2017; Oosthuizen, 2023).

Conventional air recovery models are available that were tested in steady-state on an industrial scale (Neethling and Cilliers, 2003) and dynamically on laboratory scale (Quintanilla et al., 2021c). However, the available data and lack of online measurements were not sufficient for using more complex conventional models with many parameters for state estimation, hence the less complex dynamic model of Oosthuizen (2023) was used with its already established observability and identifiability properties.

The specific contribution of the article is a reduced flotation model validated on plant data using a moving horizon estimator (MHE). The reduced model can potentially be used on an industrial circuit for a model-based supervisory control strategy such as MPC. To ensure the viability of long-term predictive control (Bergh and Yianatos, 2011), the states and parameters of the reduced model can be estimated from online measurements using an observer such as an MHE. The purpose of the reduced model is for model-based process control. As long as the model is capable of predicting the direction of change of a variable over the short term, a feedback controller can be built to control the process. Although the model does not capture all the flotation phenomena, at least in the short term, a controller in closed-loop with an estimator can reject these disturbances if variable trends are predicted correctly.

The article is structured as follows. Section 2 gives a brief overview of the analysis methods used in the study. Section 3 discusses the industrial plant and the available data. Section 4 summarises the flotation circuit model in Oosthuizen (2023) and discusses implementation shortcomings. Section 5 presents a reduced version of the model to address the shortcomings of the model in Section 4. The reduced model is used in Section 6 to develop an MHE. Section 7 shows the estimation results of the MHE and the model prediction accuracy. Section 8 concludes the article.

2. Background theory

2.1. Observability analysis theory

2.1.1. Nonlinear observability condition

For a general nonlinear state-space model

$$\dot{\mathbf{x}}(t) = f(\mathbf{x}(t), \mathbf{u}(t), \mathbf{p}), \tag{1a}$$

$$\mathbf{y}(t) = g(\mathbf{x}(t), \mathbf{u}(t)), \tag{1b}$$

the states ($\mathbf{x}(t) \in \mathbb{R}^{n_\mathbf{x}}$) are said to be *observable* if they can be inferred uniquely from the known input ($\mathbf{u}(t) \in \mathbb{R}^{n_\mathbf{u}}$) and output ($\mathbf{y}(t) \in \mathbb{R}^{n_\mathbf{y}}$) history. Similarly, the unknown parameters ($\mathbf{p} \in \mathbb{R}^{n_\mathbf{p}}$) are *identifiable* if they can be uniquely inferred from $\mathbf{y}(t)$ and $\mathbf{u}(t)$ (Villaverde et al., 2019). Importantly, these properties only indicate that the states and parameters can be estimated in theory, but do not give information regarding the practical observability of these values. This means that even if a model is observable, there is no guarantee that the states and parameters can be estimated with enough certainty to be used for MPC, given the limitations and uncertainty in the available measurement data and model. However, this analysis serves as the first step to evaluate the viability of an observer such as MHE. Note that the model assumes that $\mathbf{p}$ does not vary with time. Henceforth the "function of time" notation (t) will be dropped unless it is required for disambiguation.

The simplest check for observability of the system (1) is to check the observability (and/or identifiability) of a linear version of the model, linearised around an operating point (Seborg et al., 2011). The well-known observability matrix ($\mathcal{O}_L$) is constructed with the obtained linear state-space matrices ($\mathbf{A}$, $\mathbf{B}$, $\mathbf{C}$, $\mathbf{D}$) and the rank is evaluated (Skogestad and Postlethwaite, 2005; Antsaklis and Michel, 2007). The states are linearly observable if

$$\operatorname{rank}(\mathcal{O}_L) = n_\mathbf{x}, \tag{2}$$

The linear observability-identifiability condition (LOIC) is a sufficient and necessary condition for observability (Villaverde et al., 2019). If the LOIC is not satisfied, the states (and parameters) may still be observable in a nonlinear sense. Analogous to the linear case, the nonlinear observability-identifiability condition (NOIC) requires the evaluation of a rank condition (Hermann and Krener, 1977; Doyle and Henson, 1997; Villaverde et al., 2019). The nonlinear system in (1) is observable if:

$$\operatorname{rank}(\mathrm{d}\mathcal{O}(\mathbf{x}_0, \mathbf{u}_0)) = n_\mathbf{x}, \tag{3}$$

where the matrix $\mathrm{d}\mathcal{O}$ is constructed using Lie derivatives

$$\mathrm{d}\mathcal{O}(\mathbf{x}, \mathbf{u}) = \begin{bmatrix} \dfrac{\partial}{\partial \mathbf{x}} g(\mathbf{x}, \mathbf{u}) \\ \dfrac{\partial}{\partial \mathbf{x}} \left(L_f g(\mathbf{x}, \mathbf{u}) \right) \\ \vdots \\ \dfrac{\partial}{\partial \mathbf{x}} \left(L_f^{n_\mathbf{x}-1} g(\mathbf{x}, \mathbf{u}) \right) \end{bmatrix}. \tag{4}$$

The ith Lie derivative of g with respect to f is

$$L_f^i g(\mathbf{x}, \mathbf{u}) = \frac{\partial L_f^{i-1} g(\mathbf{x}, \mathbf{u})}{\partial \mathbf{x}} f(\mathbf{x}, \mathbf{u}) + \sum_{j=0}^{j=i-1} \frac{\partial L_f^{i-1} g(\mathbf{x}, \mathbf{u})}{\partial \mathbf{u}^{(j)}} \mathbf{u}^{(j+1)}, \tag{5}$$

where the notation $\mathbf{u}^{(j)}$ denotes the jth derivative of $\mathbf{u}$ with $\mathbf{u}^{(0)} = \mathbf{u}$ and $L_f^0 g(\mathbf{x}, \mathbf{u}) = g(\mathbf{x}, \mathbf{u})$. (If the nonlinear system in (1) is replaced with a linear system with matrices ($\mathbf{A}$, $\mathbf{B}$, $\mathbf{C}$, $\mathbf{D}$), evaluation of the NOIC using (3) and (5) will be equivalent to the LOIC in (2).)

The parameter identifiability is evaluated by expanding $\mathbf{x}$ with $\mathbf{p}$ modelled as constants. The standard state observability tests above ((2) and (3)) can then be used for the expanded system (Villaverde et al., 2019)

$$\dot{\tilde{\mathbf{x}}} = \begin{bmatrix} \dot{\mathbf{x}} \\ \dot{\mathbf{p}} \end{bmatrix} = \begin{bmatrix} f(\tilde{\mathbf{x}}, \mathbf{u}) \\ \mathbf{0} \end{bmatrix}, \tag{6a}$$

$$\mathbf{y} = g(\tilde{\mathbf{x}}, \mathbf{u}). \tag{6b}$$

2.1.2. Input excitation

The second term in (5) captures the impact of the input and its derivatives on the states and outputs. By assuming zero values for all input derivatives above a certain order, it is possible to determine the degree of input excitation required for observability (Villaverde et al., 2019).

The analysis in Oosthuizen (2023) assumed that $\mathbf{u}^{(j)} = 0 \ \forall \ j \geq 1$, implying that the analysis was done for constant inputs (all input derivatives are zero). This assumption is also made here unless explicitly stated otherwise. In the context of flotation circuits, this is a safe assumption as there are long periods of steady-state operation where inputs remain constant. This is also a more conservative approach as higher order input derivatives ($\mathbf{u}^{(j)} \neq 0$) tend to improve the system observability.

2.1.3. Identifying unobservable variables

If (3) is not satisfied and there is a rank deficiency of r_d, there are r_d unobservable states or unidentifiable parameters. If the unidentifiable parameters are excluded from $\tilde{\mathbf{x}}$ and are assumed to be known constants, it can make the remainder of the system observable.

The unobservable variables can be determined as follows. For a system with $n_{\tilde{\mathbf{x}}}$ states and parameters, the rank of $\mathrm{d}\mathcal{O}(\hat{\mathbf{x}}_0, \mathbf{u}_0)$ is taken as the maximum possible rank, $r_{\max}$. That is

$$n_{\tilde{\mathbf{x}}} = r_{\max} + r_d. \tag{7}$$

Let $\mathrm{d}\mathcal{O}_i$ denote the ith column of $\mathrm{d}\mathcal{O}$ and $\hat{x}_i$ indicate the ith state or parameter state. Next, let

$$\mathrm{d}\mathcal{O}'_j = \begin{bmatrix} \mathrm{d}\mathcal{O}_{1:j-1} & \mathrm{d}\mathcal{O}_{j+1:n_{\tilde{\mathbf{x}}}} \end{bmatrix}. \tag{8}$$

The variable $\hat{x}_j$ is possibly unobservable/unidentifiable if

$$\mathrm{rank}(\mathrm{d}\mathcal{O}'_j) = r_{\max}, \tag{9}$$

as this indicates that the jth column did not contribute to the overall matrix rank (Villaverde et al., 2019). This is done for every $\hat{x}_j$. Often (9) can hold for more than r_d variables, which implies that it is the linear combination of the variables that has a deficient rank. If r_d of these variables are assumed to be known constants, it results in an observable system.

2.2. Moving horizon estimator

Typical estimators used for nonlinear system models include the extended Kalman filter (EKF), unscented Kalman filter, particle filters (Simon, 2006) and MHE (Lucia et al., 2017). Of these, the EKF has received significant attention, especially in industrial application (Rawlings and Bakshi, 2006). However, the EKF requires linear observability and identifiability as it applies a normal Kalman filter to a linearised model at each time-step. If a model does not satisfy the LOIC, such as the model of Oosthuizen (2023), the standard EKF cannot be implemented. The MHE can deal with such systems and has the added benefit that system constraints can easily be incorporated.

The MHE uses the same state-space system as in (1), except that additive Gaussian measurement noise ($\mathbf{v}$ or $\mathbf{v}_k$) and process noise ($\mathbf{w}$ or $\mathbf{w}_k$) are added to $\mathbf{y}$ and $\mathbf{x}$, respectively (Lucia et al., 2017), and $\mathbf{p}$ represents the parameters to be estimated. The typical MHE-MPC configuration is shown in Fig. 1. For each horizon (i) of N time-steps, the optimisation problem for a discretised version of the nonlinear state-space system is given by

$$\begin{aligned} &\min_{\mathbf{x}_0, \mathbf{p}, \{\mathbf{w}_k\}_{k=0}^{N-1}} \|\mathbf{x}_0 - \hat{\mathbf{x}}_0\|^2_{\mathbf{P}_x} + \|\mathbf{p} - \hat{\mathbf{p}}\|^2_{\mathbf{P}_p} + \sum_{k=0}^{N-1} \left(\|\mathbf{v}_k\|^2_{\mathbf{P}_v} + \|\mathbf{w}_k\|^2_{\mathbf{P}_w} \right), \\ &\text{s.t.} \quad \left.\begin{aligned} &\mathbf{x}_{k+1} = f(\mathbf{x}_k, \mathbf{u}_k, \mathbf{p}, k) + \mathbf{w}_k \\ &\mathbf{y}_k = g(\mathbf{x}_k, \mathbf{u}_k, \mathbf{p}, k) + \mathbf{v}_k \\ &h(\mathbf{x}_k, \mathbf{u}_k, \mathbf{p}, k) \leq 0 \end{aligned} \right\} k = 0, \ldots, N, \end{aligned} \tag{10}$$

where $\|\mathbf{x}\|^2_{\mathbf{P}}$ denotes $\mathbf{x}^T\mathbf{P}\mathbf{x}$ and h is the function of nonlinear constraints. The MHE can be implemented using the `do-mpc` Python library (Lucia et al., 2017). Eq. (10) is solved numerically using `ipopt` in conjunction with the MA57 linear solver from the Harwell Subroutine Library (HSL) (HSL, 2013).

Only the initial states ($\mathbf{x}_0$) for each horizon are varied during optimisation, with deviation from the previous estimate of that state ($\hat{\mathbf{x}}_0$) penalised by $\mathbf{P}_x$. The values of $\mathbf{p}$ are assumed to remain constant over the entire horizon but are allowed to vary between horizons, with deviations from the previous estimate ($\hat{\mathbf{p}}$) penalised by $\mathbf{P}_p$. The states are propagated using f, with $\mathbf{w}_k$ considered an optimisation variable. The estimated $\mathbf{w}_k$ and observed $\mathbf{v}_k$ magnitudes over the entire horizon are penalised by $\mathbf{P}_w$ and $\mathbf{P}_v$ respectively. The tuning matrices ($\mathbf{P}_x$, $\mathbf{P}_p$, $\mathbf{P}_v$ and $\mathbf{P}_w$) are diagonal positive semi-definite matrices, with at least one positive definite matrix. The tuning matrices, the horizon length (N) and variable constraints play an important role in the optimisation problem solution and estimator performance.

2.3. Performance metrics

For the objective evaluation of state estimation performance, quantitative measures of performance are essential. In this work, the root mean square error (RMSE) is used as a performance metric. It is decomposed as follows:

$$RMSE = \sqrt{RMSEs^2 + RMSEu^2}, \tag{11}$$

where $RMSEs$ indicates the estimation error due to a modelling bias (systematic error) and $RMSEu$ indicates the error caused by random noise (unsystematic error). The values for $RMSEs$ and $RMSEu$ were calculated as proposed by Willmott (1981) based on a linear line of best-fit

$$\hat{P}_i = a + bO_i \tag{12}$$

on the parity plot of predictions P *vs.* observations O. The values of the two sub-metrics are calculated with

$$RMSEs = \sqrt{n^{-1} \sum_{i=1}^{n} (\hat{P}_i - O_i)^2}, \tag{13a}$$

$$RMSEu = \sqrt{n^{-1} \sum_{i=1}^{n} (P_i - \hat{P}_i)^2}. \tag{13b}$$

A high ratio between these two values

$$S/U = \frac{RMSEs}{RMSEu} \tag{14}$$

indicates the systematic component is much larger than the unsystematic component and implies poor estimation performance.

3. Plant and measurement description

3.1. Plant overview

This study considers an industrial flotation circuit which has been the subject of several studies (Venkatesan et al., 2014; Steyn and Sandrock, 2021; Horn et al., 2022). A brief overview of the flotation circuit is given below.

After being crushed in a dry section, ore is fed to a primary SAG mill which feeds into two parallel rougher banks of 7 cells each. The second rougher bank will be the focus of this work, as it only uses Dorr-Olivier forced air cells (labelled FT1–FT7 for the purposes of this study) and no naturally aspirated cells. Fig. 2 shows a simplified diagram of the second rougher bank with the available measurements and manipulated variables (MVs).

The bank is fed from a surge tank. The concentrates from the first two and last five cells are combined into two separate concentrate tanks (subscripts H_1 and H_2). Variable speed pumps on the tank outlets are used to pump the concentrates to downstream processes.

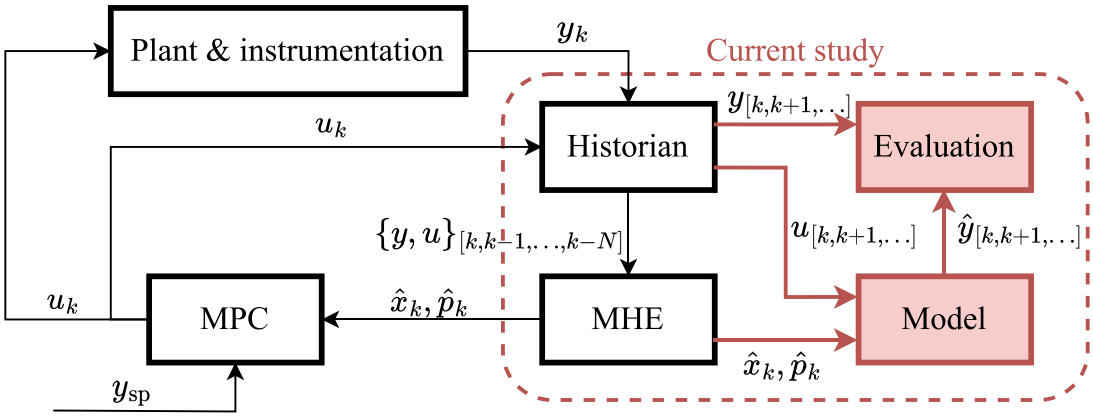

Fig. 1. The MHE-MPC set-up with parameter estimation as proposed by Oosthuizen (2023) is shown in black. The offline configuration used in the current study to evaluate the MHE performance using plant data is shown in red. (For interpretation of the references to colour in this figure legend, the reader is referred to the web version of this article.)

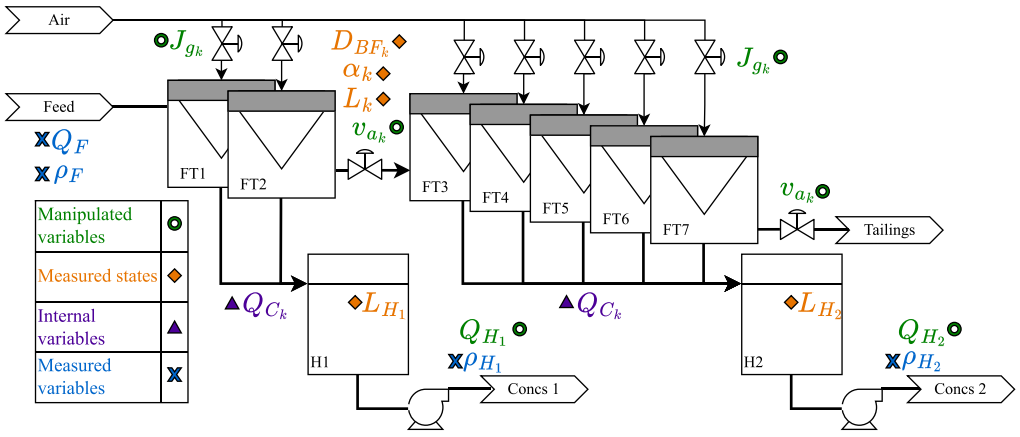

Fig. 2. The configuration of the industrial rougher bank used in this study. Variables that are applicable to multiple cells are indicated with a subscript k.

The concentrate from the first two cells can either go directly to the final concentrate or the cleaners bank. The combined concentrate of the last five cells is sent to the cleaners for further upgrading. The tailings are collected in a sump from which it is sent to a scavenger section via a secondary comminution circuit.

3.2. Available dynamic data

The data used in this study was obtained from the plant historian and the pulp sensor vendor. (The data is protected for commercial reasons. Please refer to the Appendix where data for an example system is given.)

3.2.1. Level, density and flow-rate

The cell pulp levels (L_k) are measured with a ball-float and sonar plate set-up. The concentrate tank levels (L_{H_q}) are measured with a reflective float and sonar level transducer over the entire tank height. While physical distances were used throughout, as required by the model, any level data will be reported as deviation variables for commercial reasons.

The flow-rates between cells (Q_{T_k}) are manipulated using dual dart-valves with split-range control and are not measured. The plant level controller specifies a total valve fraction ($v_{a,k}$) which is then divided between the two valves. Only the total $v_{a,k}$ value is available in the historian.

The volumetric flow-rates for the feed (Q_{F_1}), the concentrate streams (Q_{H_q}) and combined tailings (Q_T^{Tot}) are measured online. The bulk densities of these streams (ρ_F, ρ_{H_q} and ρ_T respectively) are also measured online.

3.2.2. Superficial gas velocity

The linear air velocity in the air feed pipe to each cell ($q_{air,k}$) is measured online. On the industrial plant, low-level PID controllers control $q_{air,k}$ to a set-point specified by the plant operator based on experience or calculated by an advanced process control (APC) system. Therefore, $q_{air,k}$ is different from the "true" superficial gas velocity (J_{g_k}) in the cell, which is typically used in the flotation models (Quintanilla et al., 2021c; Oosthuizen, 2023). This is due not only to the difference in pipe and cell cross-sectional areas (A_{air} and A_k), but also the varying pressure the gas is subjected to as it moves from the impeller to the top of the froth, infrequent sensor calibration, uncertainty regarding the true pipe diameter at the measurement point (Venkatesan et al., 2014). It is, therefore, necessary to determine the correct conversion between $q_{air,k}$ and J_{g_k}, as was done in previous studies (Venkatesan et al., 2014; Steyn and Sandrock, 2021) where Anglo Platinum Bubble Sizer (APBS) measurements were used.

For this study, data from image-based online pulp sensors that measure J_{g_k} directly for the first two cells in Fig. 2 was used to calibrate the conversion

$$J_{g_k} = m_{J_g,k} q_{air,k}, \tag{15}$$

where $m_{J_g,k}$ is fitted using least square regression. The online measurements of J_{g_k} were not used directly due to high levels of noise compared to measurements of $q_{air,k}$. Strictly speaking, the $q_{air,k}$ control valve fractions should be used as the MVs in the model analysis, but the dynamics from the valves to $q_{air,k}$ are assumed to be sufficiently fast to be negligible and the $q_{air,k}$ conversion to J_{g_k} was found to be sufficiently accurate to treat the calculated J_{g_k} as the MVs.

3.2.3. Air recovery

Air recovery (α_k) is the fraction of air fed to the cell (Q_{a_k}) recovered as overflowing froth, calculated as (Oosthuizen, 2023; Phillpotts et al., 2021)

$$\alpha_k = \frac{w h_{f,o,k} v_{f,o,k}}{J_{g_k} A_k}. \tag{16}$$

where w is the launder lip length, $h_{f,o,k}$ is the froth height over the lip measured by a laser froth height sensor and $v_{f,o,k}$ is the froth overflow velocity measured by a froth camera. (Note that $h_{f,o,k}$ used in (16) is different from h_{f_k} used in (18a) and (18b).)

It is assumed that the froth overflows the entire launder length of the cell at the same velocity and the same height. While unlikely, it is not possible to confirm the homogeneity of the froth from one camera per cell. The general air recovery trend should, however, remain relatively unchanged with this assumption, especially when approaching steady-state operation.

The composite nature of α_k in (16) means that it is subject to very high uncertainty as the uncertainties of all the constituent measurements are combined. High measurement noise could obscure the required dynamic information required to estimate the α_k model parameters. Errors in the measured α_k (as would be introduced by incorrect J_{g_k} measurements or non-homogeneous overflow conditions) could also pose a problem to the use of phenomenological models.

3.2.4. Froth bubble size

The top-of-froth bubble size for each cell (D_{BF_k}) is measured using froth cameras. The mean bubble size is sampled at a rate of 2 min. This sampling time is much slower than the other online measurements used, which are sampled every 10 s. To achieve the same sampling rate, the D_{BF_k} measurements were up-sampled by the historian using polynomial fit interpolation. The expected speed of the D_{BF_k} dynamics is much faster than the 2 min sampling time (Oosthuizen, 2023). The amount of dynamic information contained in the D_{BF_k} measurements is, therefore, expected to be severely limited which could complicate parameter estimation.

3.3. Static data

Currently, only 8 h shiftly composite assays, sampled every 10 min and then combined, are available for the feed of the rougher section and the individual bank tailings. The assays report on Pt, Pd and Rh (3E) content for the tails and the feed. The feed assays additionally report on the Fe content and particle size distribution. No concentrate stream assays are available for the rougher section. Unfortunately, the lab results are typically only available one to three days after the samples are taken, making the assays unusable as measurements for any real-time control or estimation purposes.

4. Model and analysis

4.1. Model description

A diagram of a single forced air flotation cell in Fig. 2 is shown in Fig. 3. The cell can be described by the dynamic model of Oosthuizen et al. (2021) and Oosthuizen (2023). As this paper is primarily concerned with the validation and not the expansion/development of the model, only a brief summary of the model equations is provided below. The model variables, inputs and parameters are summarised in Table 1, Table 2 and Table 3.

For ease of notation, let the concentration of species i and class j in tank $\triangledown$ be

$$C_{\triangledown}^{i,j} = \frac{M_{\triangledown}^{i,j}}{L_{\triangledown} A_{\triangledown}}. \tag{17}$$

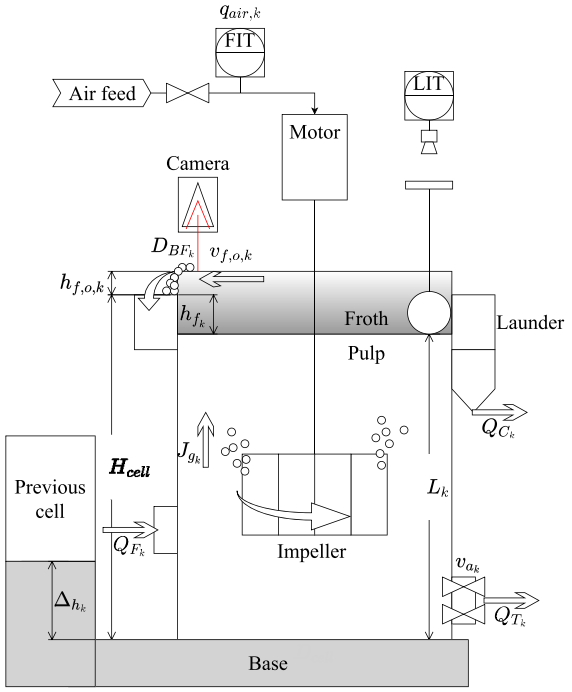

Fig. 3. Diagram of forced air flotation cell indicating the measured variables relevant to a cell and the cell dimensions.

Table 1
Model states and auxiliary variables.

Variable	Unit	Description
		Subscripts and superscripts
$\diamond$	–	Stream subscript (concentrate (C), tailings (T) and feed (F))
$\triangledown$	–	Tank subscript (hopper (H_q) or flotation cell (k))
i, j	–	Superscripts for mineral species and class
k	–	Subscript for flotation cell
		States
α_k	–	Air recovery
D_{BF_k}	mm	Mean top-of-froth bubble size
$L_{\triangledown}$	m	Tank level (cell or hopper)
$M_{\triangledown}^{i,j}$	kg	Species mass in tank $\triangledown$
		Auxiliary variables
$C_{s,\diamond}$, $C_{s,\triangledown}$	–	Mass fraction solids in stream $\diamond$ or tank $\triangledown$
$C_{\triangledown}^{i,j}$	kg m^{-3}	Concentration in tank $\triangledown$ for mineral i, j
$d_{prt}^{i,j}$	mm	Particle size for 50 % entrainment for mineral i, j
$Enr_{Frac}^{i,j}$	–	Entrainment factor for mineral i, j
h_{f_k}	mm	Froth height
λ_{air_k}	s	Froth residence time
Q_{w_k}	m^3 h^{-1}	Water recovery flow-rate
$Q_{\diamond_{\triangledown}}$	m^3 h^{-1}	Volumetric flow-rate of stream $\diamond$ to/from tank $\triangledown$
$M_{\diamond_{\triangledown}}^{i,j}$	kg h^{-1}	Mass flow-rate in stream $\diamond$ to/from tank $\triangledown$ for mineral i, j
S_{b_k}	s^{-1}	Bubble surface-area flux for cell k

The air recovery and top-of-froth bubble size for a single cell (α_k and D_{BF_k}) and the concentrate tank and mechanical cell levels (L_{H_q} and L_k) and mineral masses ($M_{H_q}^{i,j}$ and $M_k^{i,j}$) are modelled as

$$\frac{\mathrm{d}\alpha_k}{\mathrm{d}t} = \frac{K_{\alpha_{J_g}} \left(J_{g_k} - K_{0,\alpha_{J_{g_k}}} - K_{\alpha_{h_f}} h_{f_k} \right)^2 + \alpha_{OS_k} - \alpha_k}{\lambda_{\text{air}_k}}, \tag{18a}$$

Table 2
Model inputs and exogenous variables.

Variable	Unit	Description
		Inputs
J_{g_k}	mm s^{-1}	Superficial gas velocity
Q_{H_q}	m^3 h^{-1}	Concentrate flow-rate from hopper
$v_{a,k}$	–	Valve fraction
		Exogenous variables
$d_{p,\max}$	µm	Particle maximum diameter
$d_{p,\min}$	µm	Particle minimum diameter
$G^{i,j}_{F_1}$	–	Mass fraction of mineral i,j in feed solids
Φ_{s,F_1}	kg m^{-3}	Mass of solids per volume feed
Q_{F_1}	m^3 h^{-1}	Bank feed flow-rate
ρ_F	kg m^{-3}	Feed density

Table 3
Model parameters.

Symbol	Unit	Description
A_k, A_{H_q}	m^2	Cell and hopper cross-sectional area
α_{OS_k}	–	Air recovery offset
C_{PB}	–	Plateau border drag coefficient
C_{v_k}	m$^{2.5}$ h^{-1}	Valve parameter
Δ_{h_k}	m	Cell height difference
D_{OS_k}	mm	Bubble size offset
D_{BP_k}	mm	Sauter mean bubble diameter in pulp
g	m s^{-2}	Gravitational acceleration
H_{cell}	m	Cell height
k_1	–	Fluid properties parameter
$K_{0,\alpha_{J_{g_k}}}$	mm s^{-1}	Parameter related to air recovery peak
$K_{\alpha_{h_f}}$	s^{-1}	Effect of h_{f_k} on peak air recovery
$K_{\alpha_{J_g}}$	s^2 mm^{-2}	Effect of suboptimal J_{g_k} on α_k
$K_{BS_{J_g}}$	s	Effect of J_{g_k} on D_{BF_k}
K_{BS_λ}	mm s^{-1}	Effect of λ_{air_k} on D_{BF_k}
$K^{i,j}$	–	Flotation rate constant for mineral i,j
μ	Pa s	Fluid viscosity
Pe	–	Dispersion Peclet number
ρ	kg m^{-3}	Fluid density
$\rho_s^{i,j}$	kg m^{-3}	Solids density for mineral i,j

$$\frac{\mathrm{d}D_{BF_k}}{\mathrm{d}t} = \frac{K_{BS_{J_g}} J_{g_k} + K_{BS_\lambda}\lambda_{\text{air}_k} + D_{OS_k} - D_{BF_k}}{\lambda_{\text{air}_k}}, \tag{18b}$$

$$\frac{\mathrm{d}L_{H_q}}{\mathrm{d}t} = \frac{1}{A_{H_q}}\left(\sum_{k=m}^{n} Q_{C_k} - Q_{H_q}\right), \tag{18c}$$

$$\frac{\mathrm{d}L_k}{\mathrm{d}t} = \frac{1}{A_k}\left(Q_{F_k} - Q_{T_k} - Q_{C_k}\right), \tag{18d}$$

$$\frac{\mathrm{d}M^{i,j}_{H_q}}{\mathrm{d}t} = \sum_{k=a}^{b} \dot{M}^{i,j}_{C_k} - C^{i,j}_{H_q} Q_{H_q}, \tag{18e}$$

$$\frac{\mathrm{d}M^{i,j}_{k}}{\mathrm{d}t} = \dot{M}^{i,j}_{F_k} - \dot{M}^{i,j}_{C_k} - C^{i,j}_{k} Q_{T_k}, \tag{18f}$$

where Q_{F_1} is considered a measured disturbance, Q_{H_q} is taken as an MV and a and b denote the range of cells for which the concentrate is collected into tank H_q. Typically $\dot{M}^{i,j}_{F_k} = C^{i,j}_{k-1} Q_{T_{k-1}}$, except for the first cell in which case $\dot{M}^{i,j}_{F_k}$ is determined by the feed conditions using

$$\dot{M}^{i,j}_{F_1} = Q_{F_1} G^{i,j}_{F_1} \Phi_{s,F_1} \tag{19}$$

where Φ_{s,F_1} is the mass of solids per volume of feed and $G^{i,j}_{F_1}$ is the mass fraction of mineral i,j in the feed solids. The froth height (h_{f_k}) and froth residence time (λ_{air_k}) are taken as

$$h_{f_k} = 1000(H_{\text{cell}} - L_k), \tag{20a}$$

$$\lambda_{\text{air}_k} = \frac{h_{f_k}}{J_{g_k}}. \tag{20b}$$

The tailings flow-rate is given by

$$Q_{T_k} = v_{a,k} C_{v_k} \sqrt{L_k - L_{k+1} + \Delta_{h_k}}, \tag{21}$$

where $v_{a,k}$ is the valve fraction. The concentrate volumetric flow-rate (Q_{C_k}) is

$$Q_{C_k} = Q_{w_k} + \sum_{i=0}^{m}\sum_{j=0}^{n} \frac{\dot{M}^{i,j}_{C_k}}{\rho_s^{i,j}} \tag{22}$$

where the water recovery is Neethling and Cilliers (2003)

$$\frac{Q_{w_k}}{A_k} = \begin{cases} \dfrac{6.81 J^2_{g_k}}{k_1 D^2_{BF_k}}\left(1-\alpha_k\right)\alpha_k & 0 < \alpha_k < 0.5 \\ \dfrac{6.81 J^2_{g_k}}{4 k_1 D^2_{BF_k}} & \alpha_k \geq 0.5, \end{cases} \tag{23a}$$

$$k_1 = \frac{\rho g}{3\mu C_{PB}}. \tag{23b}$$

The mass flow-rates leaving a cell in the concentrate ($\dot{M}^{i,j}_{C_k}$) are calculated as

$$\dot{M}^{i,j}_{C_k} = K^{i,j} M^{i,j}_k S_{b_k} \alpha_k + Ent^{i,j}_{Frac} C^{i,j}_k Q_{w_k}, \tag{24}$$

where $K^{i,j}$ is the flotation rate constant and the bubble surface area flux (S_{b_k}) is

$$S_{b_k} = 6\frac{J_{g_k}}{D_{BP_k}}. \tag{25}$$

The entrainment factor is Oosthuizen (2023)

$$Ent^{i,j}_{Frac} = \frac{\ln\left(d^{i,j}_{prt}\right) - \ln\left(d_{p,\min}\right)}{\ln\left(d_{p,\max}\right) - \ln\left(d_{p,\min}\right)}, \tag{26}$$

where $d_{p,\min}$ and $d_{p,\max}$ are the minimum and maximum particle diameters respectively. The 50 % entrained particle diameter is

$$d^{i,j}_{prt} = \sqrt[3]{\frac{\ln(0.5) J^2_{g_k}}{K^{i,j}_{ent} h_{f_k}}}, \tag{27}$$

where

$$K^{i,j}_{ent} = \left[\frac{1}{3}\frac{g\left(\rho_s^{i,j} - \rho\right)}{18\mu}\right]^{1.5} \frac{\sqrt{k_1(\sqrt{3} - \pi/2)Pe}}{\sqrt{\alpha_k\left(1-\alpha_k\right)}}. \tag{28}$$

Eq. (28) is a simplified version of the entrainment factor model developed by Neethling and Cilliers (2009).

The empirical form of (18a) is based on the results in Hadler et al. (2010, 2012) and ensures there is a peak in α_k at an optimal J_{g_k} that is dependent on h_{f_k} (Oosthuizen, 2023). In (18a), the peak in air recovery occurs at

$$J_{g_k,\text{opt}} = K_{0,\alpha_{J_{g_k}}} + K_{\alpha_{h_f}} h_{f_k}, \tag{29}$$

where $K_{\alpha_{h_f}}$ captures the effect of h_{f_k} on the peak and $K_{0,\alpha_{J_{g_k}}}$ is the y-axis intercept for the theoretical case where $h_{f_k} = 0$. Finally, $K_{\alpha_{J_g}}$ characterises the impact of a suboptimal J_{g_k} on α_k.

The concentrate (ρ_{H_q}) and tails (ρ_T) density measurements are modelled as

$$\rho_{H_q} = \frac{\sum_{i=0}^{m}\sum_{j=0}^{n} M^{i,j}_{H_q} + \rho\left(A_{H_q} L_{H_q} - \sum_{i=0}^{m}\sum_{j=0}^{n} \frac{M^{i,j}_{H_q}}{\rho^{i,j}}\right)}{A_{H_q} L_{H_q}}, \tag{30a}$$

$$\rho_T = \frac{\sum_{i=0}^{m}\sum_{j=0}^{n} M^{i,j}_{f} + \rho\left(A_f L_f - \sum_{i=0}^{m}\sum_{j=0}^{n} \frac{M^{i,j}_{f}}{\rho^{i,j}}\right)}{A_f L_f}, \tag{30b}$$

where f denotes the final cell in the bank. The mass fraction desired mineral in concentrate solids ($G^{0,0}_{H_q}$) and tailings solids ($G^{0,0}_{T}$), i.e., the grade of the concentrate and tailings, are

$$G^{0,0}_{H_q} = \frac{M^{0,0}_{H_q}}{\sum_{i=0}^{m}\sum_{j=0}^{n} M^{i,j}_{H_q}}, \tag{31a}$$

$$G^{0,0}_{T} = \frac{M^{0,0}_{T,f}}{\sum_{i=0}^{m}\sum_{j=0}^{n} M^{i,j}_{f}}. \tag{31b}$$

4.2. Observability analysis

4.2.1. Existing analysis

Oosthuizen (2023) performed an observability analysis on the state-space model given by (18) and found that the model states

$$\mathbf{x}_1 = \left[\alpha_k, \quad D_{BF_k}, \quad L_{H_q}, \quad L_k, \quad M^{i,j}_{H_q}, \quad M^{i,j}_{k}\right]^T, \tag{32}$$

and the parameters

$$\mathbf{p}_1 = \left[\begin{array}{llll} \alpha_{OS_k}, & C_{PB}, & C_{v_k}, & D_{OS_k}, \quad K^{i,j}, \quad K_{0,\alpha_{J_{g_k}}}, \\ K_{\alpha_{h_f}}, & K_{BS_\lambda} & & \end{array}\right]^T, \tag{33}$$

are nonlinearly observable and identifiable given the inputs

$$\mathbf{u}_1 = \left[J_{g_k}, \quad Q_H, \quad v_{a,k}\right]^T, \tag{34}$$

and output

$$\mathbf{y}_1 = \left[\alpha_k, \quad D_{BF_k}, \quad L_{H_q}, \quad L_k, \quad G^{0,0}_{H_q}, \quad G^{0,0}_{T}, \quad C_{s,H_q}, \quad C_{s,T}\right]^T. \tag{35}$$

All parameters in Table 3 that are not in $\mathbf{p}_1$ in (33) are assumed to be known constants. Note that $K_{\alpha_{J_g}}$ was assumed to be a known constant as it was unidentifiable with the given model structure and available measurements. The value for $K_{BS_{J_g}}$ was also assumed to be a known constant as it would require J_{g_k} input excitation to be observable. In Venter et al. (2022) $K_{BS_{J_g}}$ is shown to have very low sensitivity relative to K_{BS_λ} and D_{OS_k}, making its exact value less important. This assumption ensures the identifiability of D_{OS_k} for each cell without requiring input excitation. Since all states and parameters are observable for this model, it should theoretically be possible to develop an online observer to estimate $\mathbf{x}_1$ and $\mathbf{p}_1$.

4.2.2. Concentrate grade measurements

Oosthuizen et al. (2021) and Oosthuizen (2023) assume that online compositional analyses of the desired mineral are available for the feed, concentrate and tailings. Removing the concentrate grade measurements for both concentrate streams of the model yields a rank deficiency of 2 with all four $M^{i,j}_{H_q}$ (assuming two mineral species and two concentrate tanks) as the possibly unobservable variables. First-order input excitation (see Section 2.1.2) could not make $M^{i,j}_{H_q}$ observable.

It was found that, at the very least, a combined concentrate grade measurement

$$G^{0,0}_{C,t} = \frac{\sum_{q=1}^{2} Q_{H_q} C^{0,0}_{H_q}}{\sum_{q=1}^{2} Q_{H_q}\left(C^{0,0}_{H_q} + C^{1,0}_{H_q}\right)}, \tag{36}$$

is required for full observability and identifiability of $\mathbf{x}_1$ and $\mathbf{p}_1$, with the output vector

$$\mathbf{y}_2 = \left[\alpha_k, \quad D_{BF_k}, \quad L_{H_q}, \quad L_k, \quad G^{0,0}_{C,t}, \quad G^{0,0}_{T}, \quad \rho_{H_q}, \quad \rho_T\right]^T. \tag{37}$$

For the vectors $\mathbf{x}_1$, $\mathbf{y}_2$, $\mathbf{p}_1$ and $\mathbf{u}_1$ for the seven cells ($k \in \{1,2,\dots,7\}$), two mineral species and one class ($i \in \{0,1\}$ and $j = 0$) and two concentrate tanks ($q \in \{1,2\}$), there are 41 states and 33 parameters to be estimated from 28 measurements and 16 MVs. The observability matrix rank results are summarised in Table 4. Table 4 shows that NOIC as per (3) is fulfilled only if the combined concentrate measurement in (36) is available. The model was linearised at steady-state and the LOIC was evaluated. Unfortunately, the LOIC as per (2) was not fulfilled. As the model is not observable at steady-state, it indicates that the system requires perturbation for the states and parameters to be observable. The more perturbation visible in the output, the quicker the estimator should be able to converge to a solution. This is not ideal in a practical sense as perturbations around steady-state operation are not ideal.

Table 4
Observability analysis results.

$L^i_f g$ order	With $G^{0,0}_{C,t}$		Without $G^{0,0}_{C,t}$	
	rank($d\mathcal{O}$)	r_d	rank($d\mathcal{O}$)	r_d
$i = 0$	28	46	27	47
$i = 1$	56	18	54	20
$i = 2$	73	1	71	3
$i = 3$	74	0	72	2
$i = 4$	74	0	72	2

Even if there is sufficient excitation and movement in the outputs, the results in Table 4 show that state and parameter estimation of the model in Section 4.1 is not possible without online compositional measurements of the concentrate from the bank sampled at a sufficiently high rate.

It is unlikely that feed-back model-based control that accounts for the recovery of different mineral species, as is desirable for flotation grade and recovery optimisation (Oosthuizen et al., 2017; Quintanilla et al., 2021a; Steyn and Sandrock, 2021; Oosthuizen, 2023), can succeed without compositional measurements.

5. Reduced model

Given the available measurements in Section 3.2 and the absence of concentrate stream compositional assays (Section 3.3), synthesising the necessary $G^{0,0}_{C,t}$ and $G^{0,0}_{T}$ at a reasonable frequency for state estimation is not possible. Therefore, the implementation of an MHE based on the full model described in Section 4.1 is not feasible. Instead, a reduced model is developed that is observable with the available measurements.

5.1. Model summary

The first two cells in the bank are the most instrumented with online J_{g_k} data and their concentrates are combined into a single concentrate tank. Furthermore, Steyn and Sandrock (2021) report that the first two cells alone achieve 61 % recovery, while the total recovery of the bank is around 64 %. This makes the first two cells a natural subsystem for a reduced model.

All solids mass balance related equations (flotation, entrainment, component balances *etc.*.) in the Oosthuizen (2023) model are removed, as their inclusion requires compositional measurements. In (23a) of the original model, the lumped parameter k_1 only accounts for the water recovery. However, in the reduced model, without the solid recovery mechanisms, an equation for water and solids recovery is required. The same form as (23a) is assumed, but with a different parameter (k_m) to account for the solids recovery as well. Thus, Q_{C_k} is given by

$$\frac{Q_{C_k}}{A_k} \approx \begin{cases} \dfrac{6.81 J^2_{g_k}}{k_m D^2_{BF_k}}\left(1-\alpha_k\right)\alpha_k & 0 < \alpha_k < 0.5 \\ \dfrac{6.81 J^2_{g_k}}{4 k_m D^2_{BF_k}} & \alpha_k \geq 0.5 \end{cases}. \tag{38}$$

The remaining equations for the reduced model are summarised in Table 5.

Removing the solids mass balance equations also necessitates removing the ρ_T and ρ_{H_q} in (30) from the set of available measurements. This prevents the estimator from using any dynamic information contained in these measurements that could contribute to better estimation results. Including the ρ_{H_1} measurement in a meaningful way requires

Table 5
Equations for the reduced model.

	Unit	Description	Equation	
			States	
α_k	–	Air recovery	$\frac{d\alpha_k}{dt} = \frac{K_{\alpha_{J_g}}\left(J_{g_k} - K_{0,\alpha_{J_{g_k}}} - K_{\alpha_{h_f}} h_{f_k}\right)^2 + \alpha_{OS_k} - \alpha_k}{\lambda_{\text{air}_k}}$	(18a)
D_{BF_k}	mm	Froth bubble size	$\frac{dD_{BF_k}}{dt} = \frac{K_{BS_{J_g}} J_{g_k} + K_{BS_\lambda} \lambda_{\text{air}_k} + D_{OS_k} - D_{BF_k}}{\lambda_{\text{air}_k}}$	(18b)
L_{H_q}	m	Hopper level	$\frac{dL_{H_q}}{dt} = \left(\sum_{k=m}^{n} Q_{C_k} - Q_{H_q}\right) / A_{H_q}$	(18c)
L_k	m	Cell level	$\frac{dL_k}{dt} = \left(Q_{F_k} - Q_{T_k} - Q_{C_k}\right) / A_k$	(18d)
			Auxiliary variables	
h_{f_k}	mm	Froth height	$h_{f_k} = 1000(H_{\text{cell}} - L_k)$	(20a)
λ_{air_k}	s	Froth residence time	$\lambda_{\text{air}_k} = \frac{h_{f_k}}{J_{g_k}}$	(20b)
Q_{C_k}	$m^3\,h^{-1}$	Concentrate flow-rate	$\frac{Q_{C_k}}{A_k} \approx \begin{cases} \frac{6.81 J_{g_k}^2}{k_m D_{BF_k}^2}\left(1-\alpha_k\right)\alpha_k & 0 < \alpha_k < 0.5 \\ \frac{6.81 J_{g_k}^2}{4 k_m D_{BF_k}^2} & \alpha_k \geq 0.5 \end{cases}$	(38)
Q_{T_k}	$m^3\,h^{-1}$	Tank outlet flow-rate	$Q_{T_k} = \upsilon_{a,k} C_{\upsilon_k} \sqrt{L_k - L_{k+1} + \Delta_{h_k}}$	(21)

at least one additional state to be added to track the percentage of the total solids in the concentrate hopper and at least one estimated parameter that quantifies the amount of solids recovered with the calculated Q_{w_k} in the form

$$Q_{C_k} = (1 + k_{sol}) Q_{w_k}. \tag{39}$$

While initial observability analysis showed that such a model reduction is observable, estimation results showed no improvement over the reduced model as summarised in Table 5. The addition of two additional states and only a single, rather noisy, measurement likely limits the amount of information possibly gained from this approach. As such, the reduced model in Table 5 was used.

Note, the purpose of the reduced model is for model-based process control. As long as the reduced model is capable of predicting the trends of the variables over the short-term, a feedback controller can be built to control the process. Although the model assumes the feed particle size distribution, chemical reagent dosages, and feed mineralogical composition remain constant, at least in the short term, a controller in closed-loop with an estimator can reject these disturbances if variable response directions are predicted correctly.

5.2. Observability results

The reduced model variable vectors used in the observability analysis are

$$\mathbf{x}_3 = \left[\alpha_k, \quad D_{BF_k}, \quad L_{H_q}, \quad L_k\right]^T, \tag{40a}$$

$$\mathbf{p}_3 = \left[\alpha_{OS_k}, \quad C_{\upsilon_k}, \quad D_{OS_k}, \quad K_{0,\alpha_{J_{g_k}}}, \quad K_{\alpha_{h_f}}, \quad K_{BS_\lambda}, \quad k_m\right]^T, \tag{40b}$$

$$\mathbf{u}_3 = \left[J_{g_k}, \quad Q_{H_q}, \quad \upsilon_{a,k}\right]^T, \tag{40c}$$

$$\mathbf{y}_3 = \left[\alpha_k, \quad D_{BF_k}, \quad L_{H_q}, \quad L_k\right]^T. \tag{40d}$$

The vectors are for two cells ($k \in 1, 2$) and one concentrate tank ($q \in 1$), resulting in 7 states, 11 estimated parameters, 7 measurements and 5 inputs. Note that $K_{BS_{J_g}}$ is assumed to be a known constant. The observability analysis results for the reduced model are summarised in Table 6. This includes the identification of the possibly unidentifiable parameters (PUPs), determined using the procedure in Section 2.1.3.

Table 6
Observability results for the reduced model.

$L_f^i g$ order	$d\mathcal{O}$ rank	r_d	PUPs	#PUPs
0	7	11	α_{OS_k}, C_{υ_k}, D_{OS_k}, $K_{0,\alpha_{J_{g_k}}}$, $K_{\alpha_{h_f}}$, K_{BS_λ}, k_m	11
1	14	4	α_{OS_k}, D_{OS_k}, $K_{0,\alpha_{J_{g_k}}}$, $K_{\alpha_{h_f}}$, K_{BS_λ}	8
2	17	1	α_{OS_k}, $K_{0,\alpha_{J_{g_k}}}$, $K_{\alpha_{h_f}}$	5
3	18	0	–	0

Table 6 shows that NOIC as per (3) is fulfilled for the reduced model. If the model is linearised, the LOIC as per (2) is not fulfilled with a rank deficiency of 4. Therefore, the states and parameters can only be estimated if the system is sufficiently perturbed.

6. MHE setup

This section describes how the MHE described in (10) is configured to estimate the states and parameters of the reduced model in Section 5 from industrial plant data discussed in Section 3.2.

6.1. Data and initialisation

A 12 h section of data containing some step changes in the J_{g_k} values was obtained from the plant. The step changes are meant to ensure that there is a large enough degree of perturbation in the output for the states and parameters to be observable. The ability of the estimator to converge to the correct state and parameter will deteriorate as the system returns to steady-state after a step in the input. An exponentially weighted moving average filter was used to reduce the amount of noise in the data. A smoothing factor value of 0.8 was used (a higher value implies less memory of the previous measurement). Given the relatively fast sampling rate for most variables, the lag introduced by the filter is expected to be minimal.

Initial parameter estimates for $\mathbf{p}_3$ were obtained by fitting the models of α_k, D_{BF_k} and Q_{T_k} ((18a), (21) and (18b), with the derivatives set equal to zero) to steady-state datapoints manually sampled from the larger dataset.

6.2. Model and constraints

The MHE in (10) was implemented with the vectors in (40). The state differential equations in Table 5 ((18a) to (18d)) represent f in (10) and the function g is the same as $\mathbf{y}_3$ in (40d).

The constraint function h consists of state and parameter constraints and additional algebraic constraints. State constraints were determined by the physical limits of the process and observed operating ranges. α_k was constrained between 0 and 1.2 (due to the observed measurements exceeding 1), D_{BF_k} was constrained between 0 mm and 120 mm (based on operating range) and the levels L_{H_1} and L_k were constrained to the physical dimensions of the cells. The lower bound for L_k was set such that the estimated h_{f_k} could not exceed the normal operating range determined by the plant operators. For the parameters, α_{OS_k} was constrained to the same range as α_k. The remaining parameters (C_{v_k}, D_{OS_k}, $K_{0,\alpha_{J_{g_k}}}$, $K_{\alpha_{h_f}}$, K_{BS_λ} and k_m) were constrained around their initially fitted values through trial and error to the largest allowed range that still resulted in reasonable estimates. $K_{\alpha_{h_f}}$, $K_{0,\alpha_{J_{g_k}}}$, K_{BS_λ} and k_m were also constrained to be positive based on the physical meaning of the parameters and observed trends in Oosthuizen (2023). Additionally, the algebraic inequality constraint

$$K_{\alpha_{J_g}}\left(J_{g_k} - K_{0,\alpha_{J_{g_k}}} - K_{\alpha_{h_f}} h_{f_k}\right)^2 + \alpha_{OS_k} \geq 0, \tag{41}$$

was placed on the estimated steady-state α_k in (18a). This ensures that the combined effect of the estimated parameters does not result in physically unrealistic steady-state α_k model predictions. This significantly improved the parameter estimation performance by restricting the possible solution space.

6.3. Sampling time and horizon

The plant has per-cell froth residence times of between 20 s and 65 s that increase down the bank. The pulp residence time is approximately 300 s per cell. Data at the plant is available at a sampling rate of 10 s. This sampling rate is also used for the MHE. In terms of the estimation horizon, a shorter horizon allows for faster tracking of changing parameters, while a longer horizon lends more noise rejection (Oosthuizen, 2023). A horizon of $N = 20$ was used.

6.4. Tuning

There are various guidelines and heuristic principles available to select the weighting matrices for MPC (Alhajeri and Soroush, 2020; Garriga and Soroush, 2010; Yamashita et al., 2023). Since MPC and MHE are similar in terms of the optimisation problem shown in (10), these principles are applicable to MHE. Unfortunately, since the objective function, the process, the requirements and aims vary for each problem, there is no formal process to select weighting matrices for MPC or MHE. Therefore, the choice of weighting matrices for the MHE implementation in this paper relied on heuristics and knowledge regarding the expected uncertainties in the data. (Although there are examples of data-driven MHEs (Nejatbakhsh Esfahani et al., 2023; Wang et al., 2024), this was not considered in this study.)

The weighting matrices are specified in Table 7 as a relative weighting value for each matrix and an operating range. The eventual diagonal matrix entry is determined by dividing the **P** entry in Table 7 by the corresponding *Range* value squared. This allows for the specification of the **P** values based on the relative uncertainties and importance of the variables and parameters without needing to constantly account for the differences in magnitude. The squared ranges are used as all the objective function terms in (10) are quadratic.

The operating ranges for the states and parameters were estimated from plant data and kept constant. The $\mathbf{P}_v$ values were initially set to low values (especially for the noisy α_k and D_{BF_k} measurements) and increased until a further increase led to poor noise rejection or significant increases in the parameter estimate variance. $\mathbf{P}_p$ values for the α_k and D_{BF_k} models ((18a) and (18b)) were set to lower values as these models are reliant on empirical parameters with limited validity ranges, but were increased if the parameter estimates displayed significant variance. The $\mathbf{P}_x$ and $\mathbf{P}_w$ values were tuned based on the prediction performance discussed in Section 7.2. High values for these weights mean that the model parameters will be changed to account for disturbances, rather than rejecting deviation of the model from the measurements as measurement noise. While this causes increased parameter and state estimate variance and reduced noise rejection, it is necessary to ensure that model predictions can track future measurements given unmodelled and unmeasured disturbances.

For this paper, weighting changes by a factor smaller than between two and five did not result in significant changes to the estimation and prediction performance. A further increase or decrease in weighting resulted in a rapid deterioration in estimation performance.

Table 7
MHE tuning parameters.

Variable	Range	$\mathbf{P}_x$	$\mathbf{P}_p$	$\mathbf{P}_v$	$\mathbf{P}_w$
α_k	0.1	0.001	–	0.01	1×10^4
D_{BF_k}	20	0.0001	–	0.1	1×10^7
L_{H_q}	0.1	1	–	100	1×10^5
L_k	0.1	1	–	100	1×10^5
α_{OS_k}	0.2	–	1	–	–
D_{OS_k}	20	–	10	–	–
C_{v_k}	1000	–	10	–	–
$K_{0,\alpha_{J_{g_k}}}$	1	–	1	–	–
$K_{\alpha_{h_f}}$	0.001	–	0.1	–	–
K_{BS_λ}	0.1	–	100	–	–
k_m	500	–	0.01	–	–

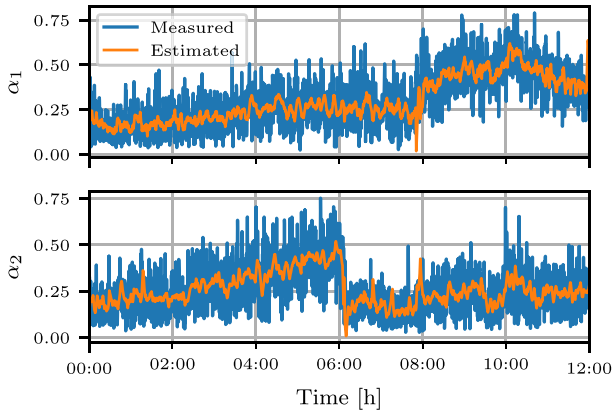

Fig. 4. State estimates for α_k.

7. Estimation and prediction performance

7.1. Estimation results

This section presents the MHE estimation results from industrial plant data. The state estimates $\mathbf{x}_3$ in (40a) compared to the measurements $\mathbf{y}_3$ in (40d) are shown in Figs. 4 to 6. The estimation errors according to (11) and (14) are shown in Table 8. The error metrics in Table 8 were calculated using the measured values of the states as the "true" values.

Considering the large uncertainty in the α_k measurements and likelihood of non-uniform overflows, the α_k estimates in Fig. 4 are reasonable. The S/U ratios for α_k in Table 8 are close to 1 which means that the systematic error is close in size to the unsystematic error. While this could indicate potential issues in the state estimation, the state estimates are relatively well-centred in the measured values and follow

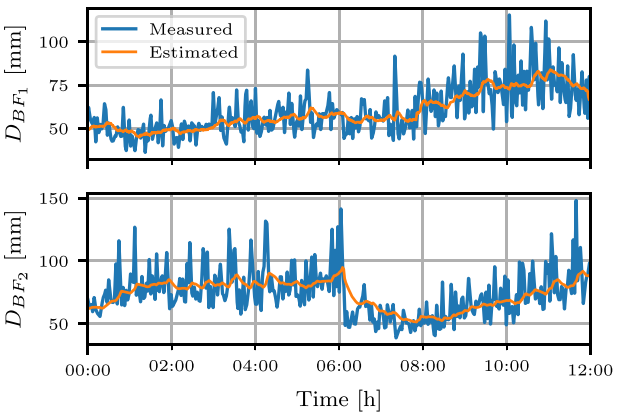

Fig. 5. State estimates for D_{BF_k}.

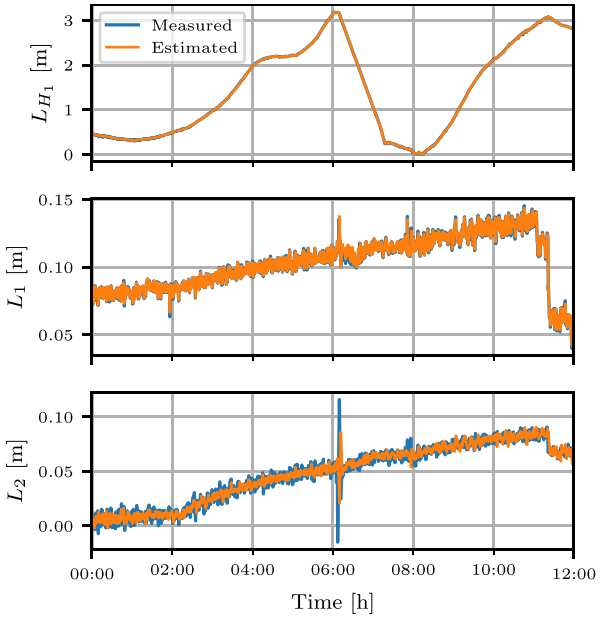

Fig. 6. State estimates for L_{H_1} and L_k.

the large obvious dynamic changes quite well. The large S/U value can in part be explained by the tendency of the state estimates to vary much less than the measurements, rejecting some actual variance in the measured values as measurement noise. Deficiency in the modelling of α_k and/or Q_{C_k} may force estimates further from the measurements in order to better fit the level measurements and volume balances. Furthermore, the estimated dynamics lag slightly behind the measured dynamics. This could indicate that the model parameters are being adjusted to account for unmodelled factors causing the movement in α_k.

The D_{BF_k} estimates shown in Fig. 5 appear to correlate relatively well with the observed dynamics. However, as seen in Table 8, the S/U ratios for the D_{BF_k} models are also close to 1 which implies inaccurate estimation. Due to the longer D_{BF_k} sampling time (see Section 3.2.4), it is more difficult to determine which D_{BF_k} movement is purely due to measurement noise rather than actual dynamics. The interpolation required for resampling also created many additional datapoints which would skew the error metrics. This would also increase the S/U ratio. As D_{BF_k} plays an integral role in the Q_{C_k} model, future investigation into the measurements and model is warranted.

The L_{H_1} and L_k state estimates in Fig. 6 followed the measurements quite closely throughout, resulting in low estimation RMSE

Table 8
Estimation and prediction error metrics.

State	Estimation		Prediction	
	RMSE	S/U	RMSE	S/U
α_1	0.10	0.70	0.11	0.65
α_2	0.10	1.05	0.11	0.99
D_{BF_1}	8.42	0.76	8.70	0.75
D_{BF_2}	12.81	1.18	13.65	1.22
L_{H_1}	0.006	0.10	0.05	0.11
L_1	0.002	0.11	0.06	0.18
L_2	0.007	0.14	0.03	0.15

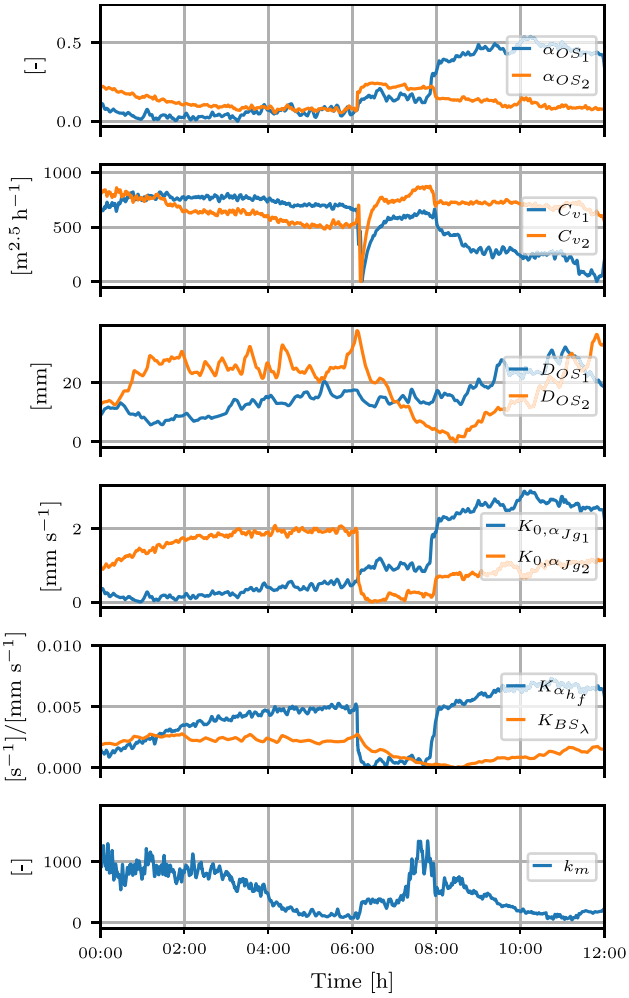

Fig. 7. Estimated parameter values over the entire dataset. All values were offset from their actual values. Note the correlation between large parameter changes and J_{g_k} steps.

values shown in Table 8 for these states. As these measurements are expected to be relatively reliable, this was deemed acceptable. Due to the measurement uncertainty of α_k and D_{BF_k}, "good" estimates of these states are expected to reject a considerable amount of variance as measurement noise.

Given the reasonable state estimation results, the parameter estimates in Fig. 7 are expected to be realistic. The parameter estimates vary considerably more and less gradually around step changes in the operating conditions than when the inputs are kept constant. The changes in α_{OS_k}, $K_{\alpha_{h_f}}$ and $K_{0,\alpha_{J_{g_k}}}$, in particular, are correlated with the J_{g_k} steps shown in Fig. 8. This indicates that the α_k model does not extrapolate very well to different operating conditions. The estimates for D_{OS_k} and K_{BS_λ} were significantly more consistent. This indicates that D_{BF_k} captures the investigated operating range reasonably well.

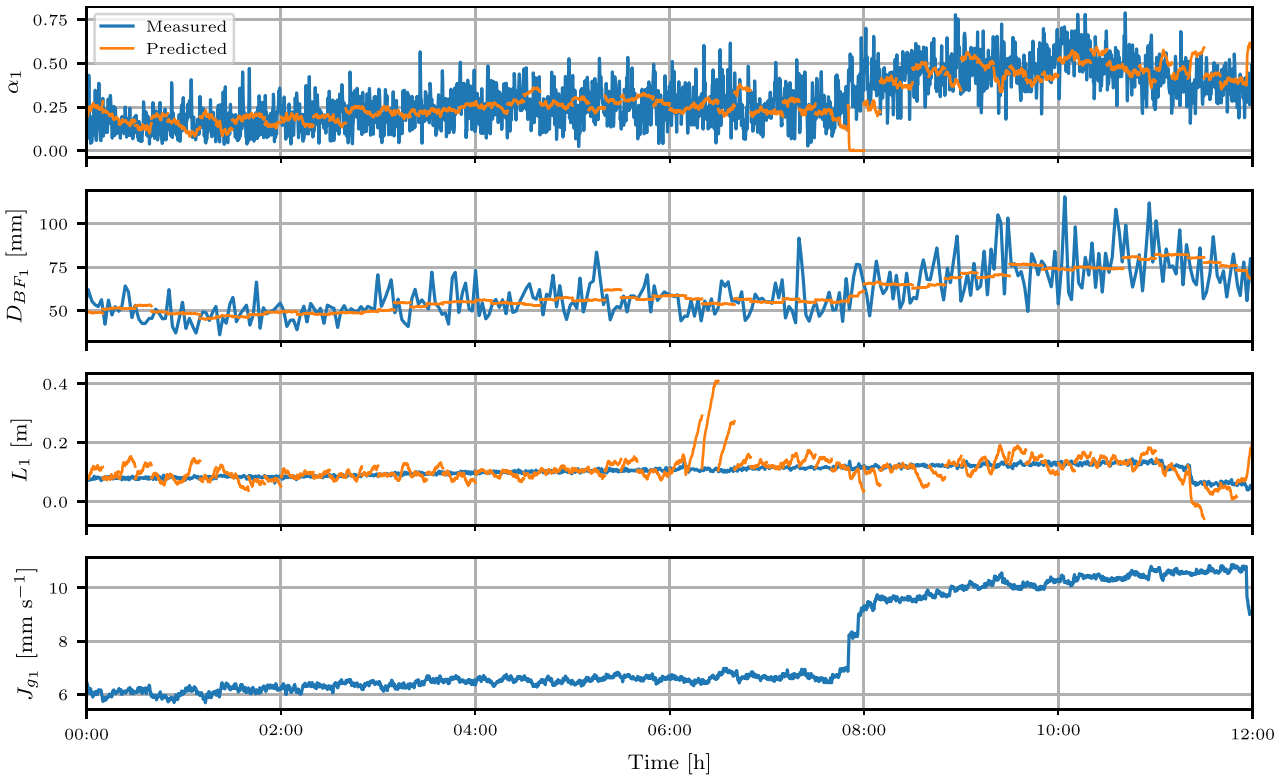

Fig. 8. FT1 state predictions initialised every 10 min. L_1 and J_{g_1} were offset from their actual values to protect sensitive operational information.

For the most part, the C_{v_k} estimates remain within a relatively narrow band, as would be expected from the valve characteristics. However, a large sudden spike in L_2 around 06:00 in Fig. 6 is accompanied by a sudden dip in both C_{v_k} estimates.

As k_m in (38) represents a combination of recovery mechanisms, a very small weight was assigned to the parameter in Table 7. Therefore, it is to be expected that this single parameter has a large variance, as seen in Fig. 7.

7.2. Prediction results

While the state and parameter estimates are mostly reasonable, the predictive accuracy of the model must also be considered. Not only will this evaluate the accuracy of the model and parameter estimates, but it will also show the feasibility of using the model for feedback control.

An MPC horizon spanning 10 min was selected. Oosthuizen (2023) implemented an MPC with a 5 min horizon and showed good control results. As the current plant dynamics are slower, a longer horizon was chosen. For the model prediction to be deemed sufficiently accurate for feedback control, it should be able to predict at least directional changes over this horizon. Any longer time horizons investigated typically resulted in worse prediction performance towards the end of the horizon (especially regarding the L_k predictions which already diverge from the measured values after 5 min in some intervals). However, any control actions for the later horizon sections would be recalculated at every time step using an updated model, making the initial prediction accuracy much more important.

The prediction accuracy over the entire section of data was tested by initialising a simulator for every 10 min section of data using the state and parameter estimates at the start of that section. The states were simulated over the rest of the section using the plant input data. No further state or parameter updates were made over the course of the simulation and the simulator did not have access to $\mathbf{w}_k$ estimates. The prediction results are shown in Figs. 8, 9 and 10. The error metrics as in (11) and (14) for the various predictions are given in Table 8.

First consider the L_k predictions in Figs. 8 and 9. The predictions are good over large sections, deviating from the measured L_k by less than 0.05 m over most of the data-set. However, the prediction sometimes diverges substantially from the measured values. Given the importance of L_k in the rest of the model equations, this will have a cascading effect on the rest of the model in such sections.

The J_{g_k} steps have an impact on D_{BF_1} and the predictions in Fig. 8 generally follow the correct trend (increasing or decreasing). However, the magnitude of the changes is often underestimated. See for example the increase in J_{g_1} around 08:00 in Fig. 8, for which a clear increase in D_{BF_1} is predicted, but the magnitude is underestimated. The RMSE values in Table 8 show that there is little difference between the estimated and predicted D_{BF_k} accuracy relative to the measured values.

The prediction quality of the α_k values in Figs. 8 and 9 are inconsistent. For example, the α_2 predictions between 00:30 and 06:30 in Fig. 9 are good and at least capture the directionality of α_2 changes. The large decrease in α_2 at 06:00 which corresponds to the decrease in J_{g_2} is predicted in the proper direction, although the magnitude of the change is overestimated. In contrast, the effect of a step change in J_{g_1} at 08:00 in Fig. 8 is predicted in the wrong direction, which indicates that the location of the optimal J_{g_k} value is on the wrong side of the measured J_{g_k}. Incorrect α_k predictions will result in incorrect Q_{C_k} values, which have a cascading effect throughout the model. The α_k model parameter estimates in Fig. 7 vary significantly. While changes in the plant dynamics are certainly expected due to changing frother dosages and other operating conditions, it is also quite possible that the parameter estimates are compensating too much for unmodelled dynamics. The S/U ratios for the α_k predictions in Table 8 are somewhat higher than desired, which aligns with the observed prediction errors. Given the parabolic nature of the optimal J_{g_k} value, the difficulty in

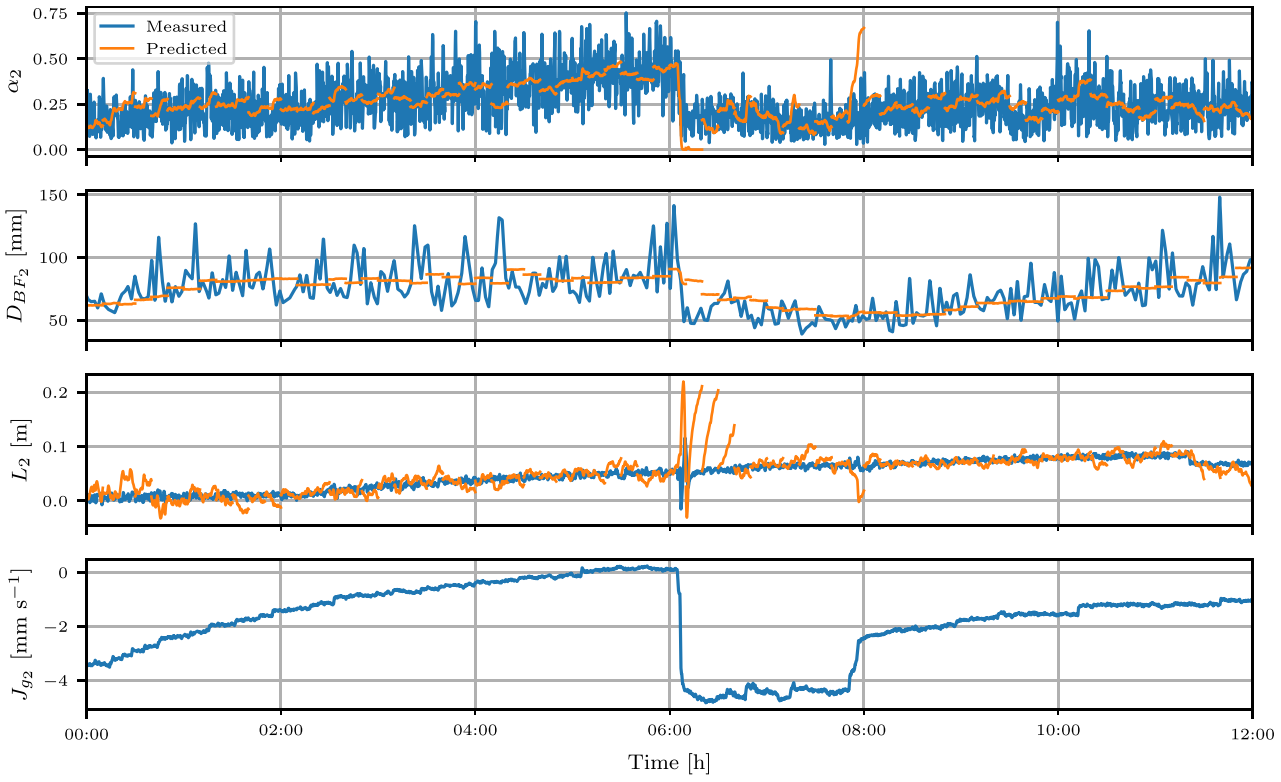

Fig. 9. FT2 state predictions initialised every 10 min. L_2 and J_{g_2} were offset from their actual values to protect sensitive operational information.

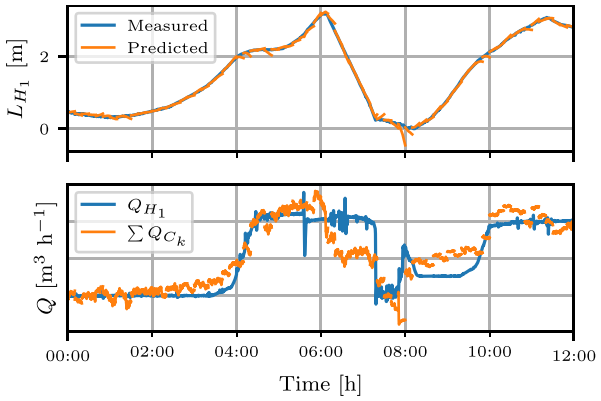

Fig. 10. L_{H_q} predictions, initialised every 10 min and the input Q_{H_1} along with the predicted $\sum Q_{C_k}$.

estimating the correct optimal J_{g_k} with few dynamics, large uncertainty in the α_k measurements and the simplified model is not unexpected.

An issue observed in both α_k and D_{BF_k} model predictions is that occasionally there are clear changes in the states, but the model predicts no change, *e.g.*, in the last 30 min of D_{BF_1} in Fig. 8. This results in the disjointed horizontal lines observed in the predictions. This is most likely due to some unmodelled factors that influence α_k and D_{BF_k} and the only tracking then achieved between horizons is due to the update of the state estimate and prediction model reinitialisation.

It is relatively easy to evaluate the accuracy of the α_k, D_{BF_k}, L_{H_q} and L_k models by comparing the predicted values to the measured values. However, without measurements of Q_{C_k} the validity of (38) has to be evaluated based on the L_{H_1} predictions, shown in Fig. 10.

The model of L_{H_1} predicts very well on sections shown in Fig. 10 where the gradient of L_{H_1} is relatively constant. The model even manages to capture the change in slope around the peak of L_{H_1} at 06:00. However, the predictions for a drastic change in gradient of L_{H_1} are less accurate (*e.g.*, at around 08:00) and the L_{H_1} prediction goes in the opposite direction from the measured values. Where the S/U ratio in Table 8 for α_k and D_{BF_k} stays roughly the same and decreases for L_k, the RMSEs and S/U values increase sharply for L_{H_1} from estimation to prediction.

8. Conclusion and recommendations

This study expanded on the work of Oosthuizen (2023) in an attempt to validate the proposed model on dynamic plant data. This included an expanded observability analysis, model reduction, the development of an MHE using the reduced model and validating the estimation performance on industrial data.

- The observability analysis showed that if online compositional measurements are available, state and parameter estimation is possible for the nonlinear model in the presence of sufficient system perturbation. However, observability is lost at steady-state operation.
- The lack of online compositional analysers, especially for the concentrate grade, severely limits the potential scope of the model and parameter estimation. Shiftly assays are unsuitable substitutes for these measurements due to the loss of dynamic information, especially since there are no concentrate grade assays. A reduced model is developed that does not require compositional measurements.

- The reduced model is observable in the nonlinear sense, but observability is lost at steady-state operation. Therefore, the system needs to be perturbed to estimate the model states and parameters. Also, the reduced model requires several simplifying assumptions that may reduce the model predictive capability and range considerably.
- The reduced model was evaluated using step-test data from an industrial plant. The steps provide the necessary perturbation to meet the observability criteria. Slightly lagging state estimates and considerable variance in the parameter estimates indicate that the parameter estimation compensates for a considerable amount of unmodelled dynamics or unmeasured disturbances.
- The model predictions over a 10 min horizon contain sections where the dynamic changes of the states are captured reasonably well and sections where the model diverges from the observed values. Eliminating the uncertainty in measurements (especially α_k) and improving parameter estimation can improve prediction accuracy.
- The plant under consideration can be regarded as a well-instrumented plant. The results indicate that it is not a trivial task to do parameter estimation using the available measurements, but that relatively simple semi-empirical models show potential for long-term model-based supervisory control.

Accurate and reliable online measurements remain essential for the success of any model-based control strategy. Online compositional measurements are relatively expensive (Brooks and Koorts, 2017), but this expense is worthwhile when compared to the benefits it provides by enabling the implementation of model-based control strategies. There is also potential for improving the state and parameter estimation through the use of alternative estimation strategies such as dual estimation (Olivier et al., 2012).

Furthermore, refining the current model or making use of alternative dynamic models should be investigated in order to better capture the system dynamics. A side-by-side comparison of the reduced model with parameter estimation and a more complex but static model such as found in Brooks and Koorts (2017) or Quintanilla et al. (2023) on the same plant data could also provide valuable insights into the value of the proposed approach, given the reliance of the parameter estimation on available measurements. In the absence of concentrate grade measurements, data-driven methods could potentially be used to augment fundamental and semi-empirical models to provide better modelling results. Ways of incorporating additional measurements, such as the concentrate density should also be investigated.

CRediT authorship contribution statement

Jaco-Louis Venter: Writing – review & editing, Writing – original draft, Visualization, Validation, Methodology, Investigation, Formal analysis, Data curation, Conceptualization. **Johan Derik le Roux:** Writing – review & editing, Validation, Supervision, Project administration, Methodology, Investigation, Formal analysis, Conceptualization. **Ian Keith Craig:** Writing – review & editing, Supervision, Project administration, Investigation, Formal analysis, Conceptualization.

Declaration of competing interest

The authors declare the following financial interests/personal relationships which may be considered as potential competing interests: Johan Derik le Roux reports financial support was provided by National Research Foundation of South Africa. If there are other authors, they declare that they have no known competing financial interests or personal relationships that could have appeared to influence the work reported in this paper.

Acknowledgements

This work is based on the research supported in part by the National Research Foundation of South Africa (Grant Number: 137769).

Appendix. Example system

The state and parameter values for the current plant are not published as they are protected for commercial reasons. To allow readers to experiment with the model as described in Section 4.1, example values are given in Tables A.9 and A.10. These values represent the steady-state operation of the system shown in Fig. A.11 consisting of two tanks ($k = 2$), one hopper ($q = 1$), two mineral species ($i \in \{0, 1\}$) and one class ($j = 1$).

The system in Fig. A.11 can be modelled in state-space form:

$$\dot{\mathbf{x}}(t) = \mathbf{f}(t, \mathbf{x}, \mathbf{u}, \mathbf{p}) \tag{A.1}$$

$$\mathbf{y}(t) = \mathbf{g}(t, \mathbf{x}, \mathbf{u}, \mathbf{p}). \tag{A.2}$$

The variables are:

- Process states (see (18)):
  $\mathbf{x} = \left[\alpha_1, \alpha_2, D_{BF_1}, D_{BF_2}, L_{H_1}, L_1, L_2, M_1^{0,0}, M_1^{1,0}, M_2^{0,0}, M_2^{1,0}, M_{H_1}^{0,0}, M_{H_1}^{1,0}\right]^T$.
- Outputs (see (30) and (31)):
  $\mathbf{y} = \left[\alpha_1, \alpha_2, D_{BF_1}, D_{BF_2}, L_{H_1}, L_1, L_2, \rho_{H_1}, \rho_T, G_H^{0,0}, G_T^{0,0}\right]^T$.
- Inputs: $\mathbf{u} = \left[J_{g_1}, J_{g_2}, Q_{F_1}, Q_{H_1}, v_{a_1}, v_{a_2}\right]^T$.
- Parameters $\mathbf{p}$ as listed in Table A.9.
- Exogenous variables as listed in Table A.10.

The auxiliary variables are:

- Froth height h_{f_k} and froth residence time λ_{air_k} (see (20)).
- Tailings flow rate Q_{T_k} (see (21)).
- Concentrate flow rate Q_{C_k} (see (22)).
- Mass concentrate flow-rate $\dot{M}_{C_k}^{i,j}$ (see (24)).

The exogenous variables in Table A.10 can be varied to allow for disturbances to the system. It is assumed the tailings of the 2-tank system flow into a third tank with a measured pulp level L_3. The initial mass flowrates, $\dot{M}_{F_1}^{i,j}$ for both species are given in Table A.10. The reduced model in Table 5 can easily be simulated by selecting the relevant parameters, variable values and equations. Regulatory controllers are required if any steps are applied to the inputs to maintain process stability.

Interested readers can contact the authors for a copy of the code.

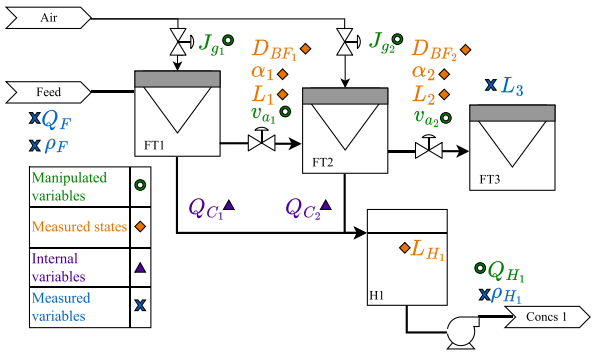

Fig. A.11. An example 2-tank system.

Table A.9
Parameter values.

Symbol	Unit	Value
Parameters		
A_k	m^2	8.82
A_{H_1}	m^2	0.2
α_{OS_1}	–	0.410
α_{OS_2}	–	0.269
C_{PB}	–	50
C_{v_k}	$m^{2.5}\,h^{-1}$	2500
Δ_{h_k}	m	0.5
D_{OS_1}	mm	9.79
D_{OS_2}	mm	6.35
D_{BP_k}	mm	0.6
g	$m\,s^{-2}$	9.81
H_{cell}	m	1.4
k_m	–	11 000
$K_{0,\alpha_{J_{g1}}}$	$mm\,s^{-1}$	7.20
$K_{0,\alpha_{J_{g2}}}$	$mm\,s^{-1}$	7.30
$K_{\alpha_{h_f}}$	s^{-1}	0.01
$K_{\alpha_{J_g}}$	$s^2\,mm^{-2}$	−0.0248
$K_{BS_{J_g}}$	s	0.529
$K_{BS_{J_g}}$	$mm\,s^{-1}$	0.313
$K^{0,0}$	–	2.3
$K^{1,0}$	–	2.142×10^{-4}
μ	Pa s	0.006
Pe	–	0.15
ρ	$kg\,m^{-3}$	1000
$\rho_s^{0,0}$	$kg\,m^{-3}$	3000
$\rho_s^{1,0}$	$kg\,m^{-3}$	2650

Table A.10
Input, exogenous variables and process state values for steady-state operation.

Symbol	Unit	Value
Inputs		
J_{g_1}	$mm\,s^{-1}$	8.4
J_{g_2}	$mm\,s^{-1}$	8.5
Q_{F_1}	$m^3\,h^{-1}$	730
Q_{H_1}	$m^3\,h^{-1}$	2.29
$v_{a,1}$	–	0.413
$v_{a,2}$	–	0.412
Exogenous variables		
$d_{p,\max}$	μm	232
$d_{p,\min}$	μm	2.77
$G_{F_1}^{0,0}$	–	0.017
$G_{F_1}^{1,0}$	–	0.983
L_3	m	1.295
$\dot{M}_{F_1}^{0,0}$	$kg\,h^{-1}$	7684
$\dot{M}_{F_1}^{1,0}$	$kg\,h^{-1}$	445 903
Φ_{s,F_1}	$kg\,m^{-3}$	621.35
Process states		
α_1	–	0.410
α_2	–	0.269
D_{BF_1}	mm	18.47
D_{BF_2}	mm	14.93
L_{H_1}	m	0.168
L_1	m	1.292
L_2	m	1.294
$M_1^{0,0}$	kg	54.1
$M_2^{0,0}$	kg	29.5
$M_1^{1,0}$	kg	6942
$M_2^{1,0}$	kg	6998
$M_{H_1}^{0,0}$	kg	15.597
$M_{H_1}^{1,0}$	kg	5.436

Data availability

The data that has been used is confidential.

References

Alhajeri, M., Soroush, M., 2020. Tuning guidelines for model-predictive control. Ind. Eng. Chem. Res. 59 (10), 4177–4191.

Antsaklis, P., Michel, A., 2007. A Linear Systems Primer. Birkhauser, Boston, MA.

Bascur Riquelme, O.A., 1982. Modelling and computer control of a flotation cell (Ph.D. thesis). The University of Utah.

Bergh, L.G., Yianatos, J.B., 2011. The long way toward multivariate predictive control of flotation processes. J. Process Control 21 (2), 226–234.

Brooks, K.S., Koorts, R., 2017. Model predictive control of a zinc flotation bank using online X-ray fluorescence analysers. IFAC-PapersOnLine 50 (1), 10214–10219.

Brooks, K., Westcott, M., Bauer, M., 2019. A combined MPC for milling and flotation – a simulation study. IFAC-PapersOnLine 52 (14), 24–29.

Doyle, F.J., Henson, M.A., 1997. Nonlinear systems theory. In: Nonlinear Process Control. Prentice Hall, Upper Saddle River, NJ, USA, pp. 111–147.

Garriga, J.L., Soroush, M., 2010. Model predictive control tuning methods: A review. Ind. Eng. Chem. Res. 49 (8), 3505–3515.

Hadler, K., Greyling, M., Plint, N., Cilliers, J.J., 2012. The effect of froth depth on air recovery and flotation performance. Miner. Eng. 36–38, 248–253.

Hadler, K., Smith, C.D., Cilliers, J.J., 2010. Recovery vs. mass pull: The link to air recovery. Miner. Eng. 23 (11–13), 994–1002.

Hermann, R., Krener, A., 1977. Nonlinear controllability and observability. IEEE Trans. Autom. Control 22 (5), 728–740.

Horn, Z.C., Haasbroek, A.L., Nienaber, E.C., Auret, L., Brooks, K.S., 2022. Comparison of online and offline pulp sensor metrics in an industrial setting. IFAC-PapersOnLine 55 (21), 91–96.

HSL, 2013. A collection of Fortran codes for large scale scientific computation. http://www.hsl.rl.ac.uk/. Last accessed on 22 February 2023.

Lucia, S., Tătulea-Codrean, A., Schoppmeyer, C., Engell, S., 2017. Rapid development of modular and sustainable nonlinear model predictive control solutions. Control Eng. Pract. 60, 51–62.

Neethling, S.J., Cilliers, J.J., 2003. Modelling flotation froths. Int. J. Miner. Process. 72 (1–4), 267–287.

Neethling, S.J., Cilliers, J.J., 2009. The entrainment factor in froth flotation: Model for particle size and other operating parameter effects. Int. J. Miner. Process. 93 (2), 141–148.

Nejatbakhsh Esfahani, H., Bahari Kordabad, A., Cai, W., Gros, S., 2023. Learning-based state estimation and control using MHE and MPC schemes with imperfect models. Eur. J. Control 73, 100880.

Olivier, L.E., Huang, B., Craig, I.K., 2012. Dual particle filters for state and parameter estimation with application to a run-of-mine ore mill. J. Process Control 22 (4), 710–717.

Oosthuizen, D.J., 2023. A dynamic flotation model for real-time control and optimisation (Ph.D. thesis). University of Pretoria.

Oosthuizen, D.J., Craig, I.K., Jämsä-Jounela, S.L., Sun, B., 2017. On the current state of flotation modelling for process control. IFAC-PapersOnLine 50 (2), 19–24.

Oosthuizen, D.J., Le Roux, J.D., Craig, I.K., 2021. A dynamic flotation model to infer process characteristics from online measurements. Miner. Eng. 167, 106878.

Phillpotts, D., Whitehead, B., Ramatsoma, S., 2021. Monitoring of air recovery for froth flotation optimisation on an industrial circuit. In: Proceedings of the XXX International Mineral Processing Congress. pp. 3348–3357.

Quintanilla, P., Navia, D., Neethling, S.J., Brito-Parada, P.R., 2023. Economic model predictive control for a rougher froth flotation cell using physics-based models. Miner. Eng. 196, 108050.

Quintanilla, P., Neethling, S.J., Brito-Parada, P.R., 2021a. Modelling for froth flotation control: A review. Miner. Eng. 162, 106718.

Quintanilla, P., Neethling, S.J., Mesa, D., Navia, D., Brito-Parada, P.R., 2021b. A dynamic flotation model for predictive control incorporating froth physics. Part II: Model calibration and validation. Miner. Eng. 173, 107190.

Quintanilla, P., Neethling, S.J., Navia, D., Brito-Parada, P.R., 2021c. A dynamic flotation model for predictive control incorporating froth physics. Part I: Model development. Miner. Eng. 173, 107192.

Rawlings, J.B., Bakshi, B.R., 2006. Particle filtering and moving horizon estimation. Comput. Chem. Eng. 30 (10), 1529–1541.

Seborg, D.E., Mellichamp, D.A., Edgar, T.F., Doyle III, F.J., 2011. Process Dynamics and Control, third ed. John Wiley & Sons.

Shean, B.J., Cilliers, J.J., 2011. A review of froth flotation control. Int. J. Miner. Process. 100 (3–4), 57–71.

Shean, B., Hadler, K., Neethling, S., Cilliers, J.J., 2018. A dynamic model for level prediction in aerated tanks. Miner. Eng. 125, 140–149.

Simon, D., 2006. Optimal State Estimation: Kalman, H_∞ and Nonlinear Approaches. Wiley-Interscience, Hoboken, New Jersey.

Skogestad, S., Postlethwaite, I., 2005. Multivariable Feedback Control: Analysis and Design, second ed. John Wiley, Chichester.

Steyn, C., Sandrock, C., 2021. Causal model of an industrial platinum flotation circuit. Control Eng. Pract. 109, 104736.

Venkatesan, L., Harris, A., Greyling, M., 2014. Optimisation of air rate and froth depth in flotation using a CCRD factorial design – PGM case study. Miner. Eng. 66–68, 221–229.
Venter, J., Le Roux, J.D., Craig, I.K., 2022. Observable dynamic models of reagent effects for model-based froth flotation control. IFAC-PapersOnLine 55 (21), 102–107.
Villaverde, A.F., Tsiantis, N., Banga, J.R., 2019. Full observability and estimation of unknown inputs, states and parameters of nonlinear biological models. J. R. Soc. Interface 16 (156), 20190043.
Wang, B., Ma, Z., Lai, S., Zhao, L., 2024. Neural moving horizon estimation for robust flight control. IEEE Trans. Robot. 40, 639–659.
Willmott, C., 1981. On the validation of models. Phys. Geogr. 2 (2), 184–194.
Yamashita, A.S., Martins, W.T., Pinto, T.V.B., Raffo, G.V., Euzébio, T.A.M., 2023. Multiobjective tuning technique for MPC in grinding circuits. IEEE Access 11, 43041–43054.